



Modelling and simulation of an alkaline electrolyser cell



Z. Abdin, C.J. Webb, E. MacA. Gray*

Queensland Micro- and Nanotechnology Centre, Griffith University, Nathan 4111, Australia

ARTICLE INFO

Article history:

Received 14 September 2016

Received in revised form

1 June 2017

Accepted 9 July 2017

Available online 12 July 2017

Keywords:

Anode

Cathode

Overpotential

Bubble effect

Separator

Electrolyte

ABSTRACT

An enhanced one-dimensional model has been developed for an alkaline electrolyser cell for hydrogen production, based on linked modular mathematical models in Simulink®. Where possible, the model parameters were derived on a physical basis and related to the materials of construction and the configuration of its components. This means that the model can be applied to many alkaline electrolyser cells, whereas existing semi-empirical models were generally developed for a specific cell. In addition to predicting the overall equilibrium electrolyser cell performance, the model is a powerful tool for understanding the contributions to cell voltage from the various internal components. It is thus useful as a guide to researchers aiming for improved performance through modified geometry and enhanced electrode materials. The model performed very well when compared to published models tested against the same sets of experimental data.

© 2017 Elsevier Ltd. All rights reserved.

1. Introduction

Worldwide hydrogen production exceeds 50 megaton (Mt) annually, principally from steam reforming of natural gas [1], which is not sustainable owing to the accompanying CO₂ emissions. Much of this hydrogen is used in petroleum refineries, for producing ammonia and other chemicals, and in food processing. A small but growing application is in filling stations for fuel-cell vehicles, with 92 new stations opened throughout the world in 2016, making a total of 274 as of January 2017 [2]. Water electrolysis is currently the most practical route for industrial-scale production of hydrogen using renewable resources [3–5], and electrolyser aimed at on-site hydrogen production for filling stations are available from numerous manufacturers.

Alkaline water electrolysis has been standard for many decades in the production of hydrogen for industrial purposes using hydroelectricity, although the commercial availability of PEM electrolyser with input powers exceeding 1 MW is breaking that monopoly. Recent surveys [6–9] of the available technologies for large scale electricity storage to mitigate problems arising from high wind power penetration into electricity grids have identified large scale alkaline electrolysis as one of the main options for storing wind energy. Compatibility with fuel cells is important for

renewable energy systems and filling stations for fuel-cell vehicles, since these involve proton exchange membrane (PEM) fuel cells that may be poisoned by impurity levels above a few parts per million (ppm) in the hydrogen stream. Alkaline electrolyser require extra purification of the product but are then able to supply hydrogen at the required purity. PEM electrolyser require careful management of membrane hydration and in this sense are less robust than the alkaline type. Alkaline electrolysis remains the cheaper alternative [10].

In an alkaline electrolyser, a high KOH concentration (25–35 wt %) in water forms the electrolyte and the hydroxide ion (OH[−]) is the charge carrier. Depending on the structure, there are two types of alkaline electrolyser cells, monopolar and bipolar. In a monopolar alkaline electrolyser, alternate electrodes are directly connected to opposite terminals of the DC power supply, making cells that are effectively in parallel. Bipolar alkaline electrolyser consist of a stack of electrodes, only the outer two of which are connected to the power supply, while the intermediate isolated electrodes act as both anode on one side and cathode on the other. In some cases the distance between the anode and cathode is about 1 mm, and these are termed zero gap alkaline electrolyser [3]. Manufacturers have generally opted for the zero-gap bipolar configuration to minimise energy consumption [5].

Over the last few years, considerable progress has been made towards improved performance of alkaline electrolyser, aiming to minimise the electricity consumption and also to increase the current density with a view to reducing the capital investment cost

* Corresponding author.

E-mail address: e.gray@griffith.edu.au (E. MacA. Gray).

Nomenclature

A	Active surface area, cm^2	p	Partial pressure, bar
C	Concentration, mol m^{-3}	ρ	Resistivity, $\Omega \text{ cm}$
D	Diffusion coefficient, $\text{m}^2 \text{ s}^{-1}$	R	Resistance (with subscript), Ω
F	Faraday constant, 96485 C mol^{-1}	R^*	Universal gas constant, $8.3144 \text{ J mol}^{-1} \text{ K}^{-1}$
G_C	Activation Energy kJ mol^{-1}	T	Temperature, K
β	Thickness of bubble zone, cm	V	Cell voltage, V
I	Current, A	X	Molar fraction
i	Current density, A cm^{-2}	δ	Thickness, mm
i_0	Exchange current density, A cm^{-2}	Γ	Diffusion collision integral
$l_{an/cat-s}$	Electrode – separator gap, cm	α	Charge transfer coefficient
$l_{an/cat-c}$	width between electrode channel to catalyst, cm	ε	Porosity
M	Molar mass, g mol^{-1}	ω	Wettability factor
\dot{N}	Molar flow rate, mol s^{-1}	τ	Tortuosity
\dot{n}	Molar flux, $\text{mol m}^{-2} \text{ s}$	Θ	Bubble coverage on the electrode surface
P	Pressure, bar	ϕ	Bubble volume fraction in electrolyte
		γ_M	Roughness factor

[5,11]. Larger units can reach a hydrogen production rate of $760 \text{ Nm}^3 \text{ h}^{-1}$ (68 kg h^{-1}), with a current density of around 0.4 A cm^{-2} and an electricity consumption of some 3.5 MW [5]. The minimum alkaline electrolyser hydrogen production level is set at 25–40% of its rated capacity. This lower limit is imposed to prevent the formation of potentially flammable mixtures of hydrogen and oxygen caused by the high diffusional flux of these gases through the separator at low currents. The operating temperature is 5–120 °C, whilst the operating pressure may vary from atmospheric up to some 10–30 bar in pressurised electrolyzers. While pressurised electrolyzers are convenient for many applications because they may avoid the need for hydrogen compression, their overall efficiency is slightly worse than that of ambient-pressure cells [12], and greater demands are placed on the separator. The role of the separator in preventing H_2/O_2 mixing is essential and its properties do influence the performance of the electrolyser via its contribution to the ohmic overpotential. The separator should exhibit high chemical and mechanical stability, low ionic resistivity and high wettability. Moreover, it must withstand extreme conditions: a strong alkaline environment at elevated temperature. Porous composite materials based on polymers (e.g. polysulfone) and ceramics (e.g. ZrO_2 particles) have been developed to replace the formerly common asbestos separators. Among the newer materials, Zirfon® is a micro-porous organo-mineral material containing a mixture of a hydrophilic ZrO_2 powder (85 wt%) and polysulfone (15 wt%), with high surface area ($22 \text{ m}^2/\text{g}$) and optimum wettability [13].

This paper continues a series in which mutually compatible modular models of the components of an energy system, specifically one incorporating solar-derived hydrogen [14], are presented. One overall objective is to link the suite of component models together to form a whole-of-system model and simulation that can realistically predict the behaviour of a planned energy system, as a prerequisite to specifying the characteristics and capacities (sizes) of its components. Alternatively, such a model can simulate the behaviour of an existing energy system for research and other purposes, such as on-the-fly prediction of the trajectory of the energy system as its input(s) and load(s) change in real time. The component models are realised, without the use of finite-element analysis, in Simulink®. The first two such models are for a PEM electrolyser cell [15] and a PEM fuel cell [16]. The next, for an alkaline electrolyser cell, is presented here.

A second very important objective of the work is to use the

component models as research tools to predict the effects of influential design parameters, materials and environmental conditions, thus lessening the need for experimentation, which is expensive and time-consuming.

Design parameters are necessarily physical in nature, that is, related to dimensions, materials properties and theory that represents measurable reality. On the other hand, most of the presently available models in this field take a semi-empirical approach, representing the characteristics of the electrolyser (or fuel cell) through equations containing empirical terms and coefficients that lack any direct relationship to physical reality. This creates a disconnect between design and measured performance. The key to achieving the second objective is therefore to place the equations that embody the characteristics of the various elements of the electrolyser, fuel cell *etc.* on a proper physical basis by embedding the theory of the underlying physical mechanisms. Doing this has significant advantages. Firstly, it makes the model more generic in its application, in contrast to the present general reliance on empirical equations that only describe the characteristics of the particular component under consideration, perhaps with no applicability to the greater class of such components. Secondly, a sound physical basis for the model better allows the effects of changing materials, dimensions *etc.* to be predicted in the quest for enhanced performance, by performing sensitivity analyses, for instance, as was demonstrated for the PEM electrolyser cell [15].

A third benefit is that a realistic model may be used to diagnose problems in the modelled component or system via changes in the fitted parameters arising from, for instance, degradation of an electrode, potentially allowing the degradation to be traced to its physical origin.

Current approaches to modelling alkaline electrolyzers range from purely empirical representations at the system level as a “black box” with fixed conversion efficiency calculated from experimental values for the hydrogen production and electricity consumption rates (e.g. Ref. [17]) to very low-level studies of internal processes. An example of the latter is the model of El-Askary *et al.*, who considered bubbly two-phase flow in a mathematical model based on Eulerian–Eulerian two-fluids solved by the SIMPLE algorithm [18]. Historically, the mainstream of modelling work has been carried out between these limits, directed to modelling the electrochemical behaviour of an electrolyser cell by representing the processes that contribute to its polarisation curve with a mixture of theory and empiricism.

Much of the earlier modelling of alkaline electrolyzers in the literature was related to solar-hydrogen demonstration projects. Perhaps the most detailed model of an alkaline electrolyser was developed within the SIMELINT program as a part of the Saudi Arabian–German HYSOLAR-project [19]. This model was validated against experimental data and predicted the thermal behaviour, cell voltage, gas purities and efficiencies for any given power. Other empirical models have also been developed [20–24], but these have either been less detailed or not tested and verified against experimental data. In fact models based on empirical parameters typically only described the current and voltage characteristics [23,24]. In the early 90s more realistic models of alkaline electrolyzers began to appear [19,25]. The semi-empirical approach taken can describe the characteristics of the polarisation curve reasonably well when linked with a linear model of dependence on environmental parameters. Employing a similar tactic, Ulleberg [11] proposed a model with nonlinear functions of temperature, which proved effective in emulating its influence on the polarisation curve.

Most of the developed models [11,19] were tried to the characteristics of specific electrolyzers and did not account for the effects of pressure, electrolyte concentration and bubbles in the bulk electrolyte and on the electrode surface. Agbossou *et al.* [26,27] developed a multi-physics model based on identification of phenomena observed during operation. This model offers insight to the causes of malfunctions in the electrolyser and aids optimization of the operation of the electrolyser.

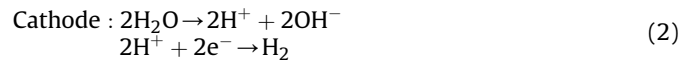
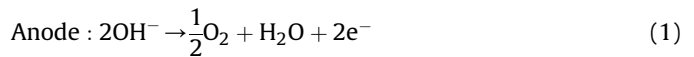
Generally, a multi-dimensional model is useful to understand the details of the individual components of an alkaline electrolyser cell in order to optimise the mechanical and electrical design, but if extrapolated to the scale of an entire hybrid energy system this approach would be very cumbersome. Thus, simplified modelling and simulation may play a significant role in engineering complex systems. This reasoning also applies to the transient behaviour, which in a real electrolyser is largely determined by thermal effects, relative to which the transient response of an isolated cell is found experimentally to be fast [28]. In this study, a detailed simplified, steady-state model for an alkaline electrolyser cell has been developed and tested against published experimental results. The computational demands are small enough for it to be embedded in a whole-of-electrolyser model within a simulation of the entire energy system.

The approach adopted insists on a physical basis for the model parameters where possible. The model includes material balance and mole balance in the anode and the cathode subsystems. The effective binary diffusion through the porous electrodes was modelled, employing calculated diffusivities corrected for porosity, tortuosity and transport through the electrolyte, based on experimentally and analytically determined transport properties. This model factors-in the mechanism of molar concentration at the electrode–electrolyte interface and takes into account the resistances of the electrodes, electrolyte and separator, including bubble effects. The physically based parameterisation of the model exposes the relative contributions of the various overpotentials to the polarisation curve in detail. Applying the model to data from a real electrolyser cell can thus help to understand how cell components influence the electrolyser performance and suggest directions for further research to improve performance.

2. Model development

In the alkaline water electrolyser cell (Fig. 1), the anode and cathode are immersed in conductive electrolyte.

The reactions at the anode and the cathode are



Under the influence of the electric field developed by the applied potential difference (voltage), hydrogen ions (H^+) move towards the cathode, while hydroxide ions (OH^-) move towards the anode. A gas separator with good ionic conductivity prevents the oxygen and hydrogen gases generated from mixing. Gas receivers are used to collect the hydrogen and oxygen.

The separator is one point of difference between the alkaline and PEM electrolyser types. Another is the liquid electrolyte and the existence of bubbles adjacent to the electrodes. The porous electrodes, bubble zones and the porous separator are examples of inhomogeneous conductors, whose effective conductivities can be mathematically related to their physical distribution of pores or bubbles.

Typically, the bubble coverage depends on the current density, electrolyte fluid properties, electrode surface characteristics, temperature and pressure. Particularly at higher current densities, increased bubble coverage contributes significantly to the activation overpotential by rendering the covered portion of the electrode electrochemically inactive.

In general, make-up water is continuously added to the system to maintain constant electrolyte concentration and viscosity. Electrolyte circulation is useful in limiting the concentration gradient, detaching bubbles from the electrodes and distributing heat through the electrolyser cell.

The model of an alkaline electrolyser cell presented here is built up from three principal modular components, called ancillaries in Simulink, labelled here *anode*, *cathode* and *voltage*. In the following subsections detailing the ancillaries, the mechanisms that control the operation of the cell are modelled in terms of physically meaningful parameters where feasible. An exception is bubble coverage of the electrodes, where qualitative understanding of bubble phenomena has not yet translated into a quantitatively predictive model [29]. Here it is assumed that the bubbles are identical, uniformly distributed through the (identical) bubble zones and across the electrode surface, with the same shape (segmented sphere) and residence time on the electrode surface, and the same break-off size.

In a real electrolyser the spacing between the elements is small compared to their extent perpendicular to the current path. Therefore the active areas of the anode and cathode are taken to be the same, implying that the current density is the same at each electrode.

2.1. Anode ancillary

At the anode, hydroxide ions are oxidized according to Eq. (1) to produce oxygen, electrons and water. The mole balance equations for the anode are

$$\frac{dN_{\text{H}_2\text{O}}}{dt} = \dot{N}_{\text{H}_2\text{O}}^{\text{in}} - \dot{N}_{\text{H}_2\text{O}}^{\text{out}} + \dot{N}_{\text{H}_2\text{O}}^{\text{gn}} \quad (3)$$

$$\frac{dN_{\text{O}_2}}{dt} = \dot{N}_{\text{O}_2}^{\text{in}} - \dot{N}_{\text{O}_2}^{\text{out}} + \dot{N}_{\text{O}_2}^{\text{gn}} \quad (4)$$

where $\dot{N}_{\text{O}_2}^{\text{in}}$, $\dot{N}_{\text{H}_2\text{O}}^{\text{in}}$, $\dot{N}_{\text{O}_2}^{\text{out}}$, $\dot{N}_{\text{H}_2\text{O}}^{\text{out}}$ are anode inlet and outlet molar flow rates of oxygen and water respectively and $\dot{N}_{\text{O}_2}^{\text{gn}}$, $\dot{N}_{\text{H}_2\text{O}}^{\text{gn}}$ are the molar

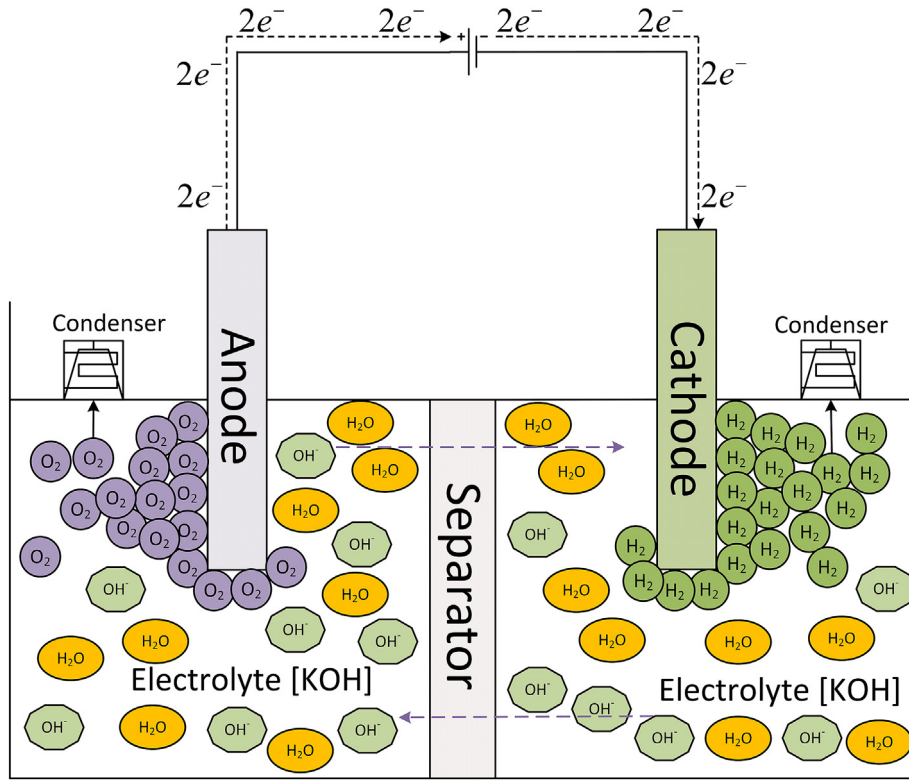


Fig. 1. Schematic of the alkaline electrolyser cell.

flow rates of oxygen and water generation at the anode.

According to Faraday's law the molar flow rates of oxygen and water at the anode side are

$$\dot{N}_{O_2}^{gn} = \frac{I}{4F} \quad (5)$$

$$\dot{N}_{H_2O}^{gn} = \frac{I}{2F} \quad (6)$$

where F is the Faraday constant and I is the current through the cell. The current is implicitly assumed to be uniformly distributed by virtue of the model being one-dimensional,

$$I = iA_e \quad (7)$$

where i is the current density and A_e is the (external) electrode surface area.

The molar flux of water through the anode can be expressed as

$$\dot{n}_{H_2O}^{an} = \frac{\dot{N}_{H_2O}^{gn}}{A_e} = \frac{I}{2FA_e} = \frac{i}{2F} \quad (8)$$

and the molar flux of oxygen through the anode can be expressed as

$$\dot{n}_{O_2}^{an} = \frac{\dot{N}_{O_2}^{gn}}{A_e} = \frac{I}{4FA_e} = \frac{i}{4F} \quad (9)$$

Since the sum of the molar fractions at the anode is $X_{H_2O} + X_{O_2} = 1$, the effective partial pressure of O_2 is

$$p_{O_2} = \frac{p_{H_2O}}{X_{H_2O}} (1 - X_{H_2O}) \quad (10)$$

Here it has been assumed that the gases present (H_2 and $H_2O(g)$ at the anode; O_2 and $H_2O(g)$ at the cathode) are ideal and uniformly distributed, and the pressure is uniform throughout the electrode gas flow channels. Taken together with the assumption of 1D geometry, these assumptions justify simplification the Stefan-Maxwell equation [30] by setting the molar flux of water vapour normal to the surface of the anode to zero [31]. The one-dimensional gradient of the molar fraction of water at the anode may then be simply expressed as

$$\frac{dX_{H_2O}}{dx} = \frac{\epsilon_{an}}{\tau_{an}} \frac{R^* T i}{2FP_{an} D_{eff}^{an}} \quad (11)$$

Now integrating Eq. (11) from the anode channel to the catalyst surface gives

$$X_{H_2O} = \frac{\epsilon_{an}}{\tau_{an}} \exp\left(\frac{R^* T l_{an-c} i}{2FP_{an} D_{eff}^{an}}\right) \quad (12)$$

where P_{an} is the anode pressure, ϵ_{an}/τ_{an} is the ratio of electrode porosity to tortuosity, l_{an-c} is the anode channel-to-catalyst distance and D_{eff}^{an} is the effective binary (O_2 – H_2O) diffusion coefficient at the anode. A detailed explanation of effective binary diffusion is given in § 2.3.3. Saturation of the electrode gases with water vapour also implies that the effective anode water pressure is the saturated vapour pressure $P_{H_2O,KOH}^{sat}(T)$. The calculation of the vapour pressure of the KOH solution can be found elsewhere [32]. Therefore, the partial pressure of oxygen at anode can be written as

$$p_{O_2} = \left[1 / \frac{\epsilon_{an}}{\tau_{an}} \exp\left(\frac{R^* T l_{an-c} i}{2FP_{an} D_{eff}^{an}}\right) - 1 \right] P_{H_2O,KOH}^{sat}(T) \quad (13)$$

2.2. Cathode ancillary

At the cathode, water is reduced according to Eq. (2) to produce protons and hydroxide ions, and the protons combine with electrons to form hydrogen. The mole balance equations for the cathode ancillary are

$$\frac{dN_{H_2O}}{dt} = \dot{N}_{H_2O}^{in} - \dot{N}_{H_2O}^{out} - \dot{N}_{H_2O}^{cons} \quad (14)$$

$$\frac{dN_{H_2}}{dt} = \dot{N}_{H_2}^{in} - \dot{N}_{H_2}^{out} + \dot{N}_{H_2}^{gn} \quad (15)$$

where $\dot{N}_{H_2}^{in}$, $\dot{N}_{H_2O}^{in}$, $\dot{N}_{H_2}^{out}$ and $\dot{N}_{H_2O}^{out}$ are the cathode inlet and outlet molar flow rates of hydrogen and water respectively, $\dot{N}_{H_2O}^{cons}$ is the molar flow rate of water consumption at the cathode and $\dot{N}_{H_2}^{gn}$ is the molar flow rate of hydrogen generation at the cathode.

According to Faraday's law

$$\dot{N}_{H_2}^{gn} = \frac{I}{2F} \quad (16)$$

and

$$\dot{N}_{H_2O}^{cons} = \frac{I}{2F} \quad (17)$$

The molar fluxes of hydrogen and water at the cathode can be expressed as

$$\dot{n}_{H_2}^{cat} = \frac{\dot{N}_{H_2}^{gn}}{A_e} = \frac{I}{2FA_e} = \frac{i}{2F} \quad (18)$$

$$\dot{n}_{H_2O}^{cat} = \frac{\dot{N}_{H_2O}^{cons}}{A_e} = \frac{I}{2FA_e} = \frac{i}{2F} \quad (19)$$

The effective partial pressure of hydrogen at the cathode can be expressed as

$$p_{H_2} = \frac{p_{H_2O}}{X_{H_2O}} (1 - X_{H_2O}) \quad (20)$$

Calculating the molar fraction of water at the cathode as for the anode and rearranging Eq. (20) gives

$$p_{H_2} = \left[1 - \frac{\epsilon_{cat}}{\tau_{cat}} \exp\left(\frac{R^*T}{2FP_{cat}D_{eff}^{cat}} l_{cat-c} i\right) - 1 \right] P_{H_2O,KOH}^{sat}(T) \quad (21)$$

where P_{cat} is the cathode pressure, l_{cat-c} is the distance between cathode channel to catalyst and D_{eff}^{cat} is the effective binary (H_2-H_2O) diffusion coefficient at the cathode.

2.3. Voltage ancillary

Water splitting by thermolysis is thermodynamically unfavourable at ambient temperature. Providing the necessary energy via electrolysis under adiabatic conditions therefore requires the total reaction enthalpy to be supplied by the electric current. In this case, the thermo-neutral voltage ($V_{tn} = 1.48$ V at 25 °C and 1 atm) is needed to maintain the electrochemical reaction without heat transfer [33]. Below the thermo-neutral voltage the reaction is endothermic, and is exothermic above it. Some of this excess energy appears as lossy contributions to the cell overpotential. An overpotential is also necessary to achieve useful reaction rates for activated steps in the overall reaction mechanism [34,35] and provide

thermodynamic drive for diffusion at the electrodes. The standard or reversible cell voltage is $V_{std}^0 = 1.229$ V at 25 °C and 1 atm. The difference between V_{tn} and V_{std}^0 corresponds to the entropy contribution to the total change in free energy, +237.2 kJ mol⁻¹ [36]. This is the least necessary amount of electrical energy to produce hydrogen and oxygen at 25 °C and 1 atm. Accordingly, the cell voltage can be written as

$$V = V_{oc} + V_{act} + V_{con} + V_{ohm} \quad (22)$$

where V_{oc} is the open-circuit voltage, V_{act} is the activation overpotential, V_{con} is the concentration overpotential and V_{ohm} is the ohmic overpotential.

2.3.1. Open-circuit voltage

The equilibrium or open-circuit cell voltage falls as the temperature increases via the entropy contribution and rises as the pressure rises via the free energy of the produced gases. For water electrolysis the open-circuit voltage (OCV) may be obtained from the Nernst equation as follows [37,38]

$$V_{oc} = V_{std}^0 + (T - T_{ref}) \times \frac{\Delta S^0}{nF} + \frac{R^*T}{2F} \left[\ln\left(\frac{p_{H_2} \sqrt{p_{O_2}}}{a_{H_2O, KOH}}\right) \right] \quad (23)$$

The second term in Eq (23) is added to account approximately for the change in the reversible voltage at temperatures different from the standard reference temperature [37,38]. Here $\Delta S^0/nF$ (-0.9×10^{-3} J (mol.K)⁻¹) is the standard state entropy change and $a_{H_2O,KOH}$ is the water activity of the electrolyte solution.

2.3.2. Activation overpotential

The electrode kinetics is embodied in the activation overpotential, arising in the transfer of charge between the electrodes and chemical species. The nature and pre-treatment of the electrode surface and the composition of the electrolytic solution adjacent to the electrode determine the rate of the electrode reaction.

Applying transition-state theory and assuming a single rate-limiting activated step in the complex reaction mechanism at each electrode leads to the well-known Butler–Volmer equation, by means of which the activation overpotentials for the anode and cathode may be written

$$V_{act}^{an} = \frac{R^*T}{\alpha_{an}F} \ln\left(\frac{i}{i_0^{an}}\right) \quad (24)$$

$$V_{act}^{cat} = \frac{R^*T}{\alpha_{cat}F} \ln\left(\frac{i}{i_0^{cat}}\right) \quad (25)$$

Here α is the charge transfer coefficient for electrode, i is the current density and i_0 is the effective exchange current density of the electrode. It is assumed that the electrode areas are equal, so conserving the cell current implies equal current densities at the anode and cathode. The effective exchange current density depends on the temperature at the surface of the electrode and on the roughness factor, which is defined as the effective electrode area (electrochemical) divided by the geometrical area. The reference exchange current density (at reference temperature and pressure) depends in the available catalyst surface area, so the effective exchange current density at any temperature may be expressed, assuming an activated mechanism, by Refs. [39,40]:

$$i_0 = \gamma_M \exp \left[-\frac{\Delta G_C}{R^*} \left(\frac{1}{T} - \frac{1}{T_{ref}} \right) \right] i_{0,ref} \quad (26)$$

where γ_M is the electrode roughness factor, $i_{0,ref}$ is the reference exchange current density at temperature T_{ref} and ΔG_C is the free energy of activation.

Bubbles adhered to the electrode surface isolate the covered fraction of the surface from the reacting species and render it inactive. This effect may be included by re-scaling the area contributing to the current density in Eqs (24) and (25), giving an additional contribution to the overpotential owing to bubble coverage:

$$V_{act}^{an} = \frac{R^*T}{\alpha_{an}F} \ln \left(\frac{i}{i_0^{an}} \right) + \frac{R^*T}{\alpha_{an}F} \ln \left(\frac{1}{1 - \Theta_{an}} \right) \quad (27)$$

$$V_{act}^{cat} = \frac{R^*T}{\alpha_{cat}F} \ln \left(\frac{i}{i_0^{cat}} \right) + \frac{R^*T}{\alpha_{cat}F} \ln \left(\frac{1}{1 - \Theta_{cat}} \right) \quad (28)$$

Rearranging Eqs (27) and (28)

$$V_{act}^{an} = \frac{R^*T}{\alpha_{an}F} \ln \left(\frac{i}{i_0^{an}(1 - \Theta_{an})} \right) \quad (29)$$

$$V_{act}^{cat} = \frac{R^*T}{\alpha_{cat}F} \ln \left(\frac{i}{i_0^{cat}(1 - \Theta_{cat})} \right) \quad (30)$$

where Θ is the fractional bubble coverage on the electrode surface.

Calculating the bubble coverage of an electrode from first principles is a very complex problem, since the bubble effect depends on the surface characteristics of the electrode, the surface tension of the electrolyte, and natural or forced circulation of the electrolyte, all of which influence the size at which the bubbles detach from electrode surface. A mathematical model developed by Vogt and Balzer [29] is regarded as only indicative by its authors. Therefore an empirical expression has been employed for bubble coverage as a function of current density and temperature and modified for the effect of pressure [29,41]:

$$\Theta = \left[-97.25 + 182 \frac{T}{T_{ref}} - 84 \left(\frac{T}{T_{ref}} \right)^2 \right] \times \left(\frac{i}{i_{lim}} \right)^{0.3} \times \frac{P}{P - P_{H_2O,KOH}^{sat}(T)} \quad (31)$$

Here i_{lim} is the limiting current density at 100% bubble coverage with typical value 300 kAm^{-2} [29,42].

2.3.3. Concentration (diffusion) overpotential

A concentration or diffusion overpotential develops because of a gradient in the reactant concentration in the vicinity of the electrode surface, which arises because of the electrochemical reactions taking place. The mass flow through the porous electrodes is typically explained as a diffusion phenomenon, which may be modelled by Fick's law. It is apparent from Eqs (1) and (2) that water electrolysis involves binary chemical systems. In such a mixture, each species can be quantified in terms of its density or molar concentration. To predict the voltage loss due to the reactant concentration gradient, the Nernst equation may be combined with Fick's law to model the diffusion rate [15].

Fig. 2 illustrates the species concentrations and the molar fluxes inside an alkaline electrolyser cell. Now applying Fick's law, at the

electrode–electrolyte interface the molar concentration of gases can be written as

$$\dot{n}_{O_2} = D_{eff}^{an} \frac{(C_{O_2,el} - C_{O_2,ch})}{\delta_{an}} \quad (32)$$

$$\dot{n}_{H_2} = D_{eff}^{cat} \frac{(C_{H_2,el} - C_{H_2,ch})}{\delta_{cat}} \quad (33)$$

After rearranging Eqs (32) and (33)

$$C_{O_2,el}^{an} = C_{O_2,ch} + \frac{\delta_{an} \dot{n}_{O_2}}{D_{eff}^{an}} \quad (34)$$

$$C_{H_2,el}^{cat} = C_{H_2,ch} + \frac{\delta_{cat} \dot{n}_{H_2}}{D_{eff}^{cat}} \quad (35)$$

At the pressures typical of alkaline electrolyser operation, the molar concentration of a gaseous species is related to its partial pressure through the ideal gas law. Then the molar concentrations at the electrode–electrolyte interfaces (Eqs (34) and (35)) can be written as

$$C_{O_2,el}^{an} = \frac{P_{an} X_{O_2}}{R^*T} + \frac{\delta_{an} \dot{n}_{O_2}}{D_{eff}^{an}} \quad (36)$$

$$C_{H_2,el}^{cat} = \frac{P_{cat} X_{H_2}}{R^*T} + \frac{\delta_{cat} \dot{n}_{H_2}}{D_{eff}^{cat}} \quad (37)$$

where δ_{an} and δ_{cat} are the thicknesses of the anode and cathode. The first term in Eqs (36) and (37) represents the molar concentration of oxygen and hydrogen in the electrode channel and the second term represents the molar concentration of these gases in the porous electrode.

Diffusion of a molecular species with mean free path $\bar{\lambda}$ through a porous medium with average pore radius \bar{r} occurs by two principal mechanisms: molecular diffusion for $\bar{r} > \bar{\lambda}$ and Knudsen diffusion for $\bar{r} < \bar{\lambda}$, when interactions with the pore wall occur much more frequently than collisions with other molecules. In most porous structures, both mechanisms are significant [43], so the effective binary diffusion coefficients at the anode and cathode can be expressed as [43]

$$\frac{1}{D_{eff}^{an}} = \frac{\epsilon_{an}}{\tau_{an}} \left(\frac{1}{D_{eff}^{O_2-H_2O}} + \frac{1}{D_{eff}^{H_2O,K}} \right) \quad (38)$$

$$\frac{1}{D_{eff}^{cat}} = \frac{\epsilon_{cat}}{\tau_{cat}} \left(\frac{1}{D_{eff}^{H_2-H_2O}} + \frac{1}{D_{eff}^{H_2O,K}} \right) \quad (39)$$

where $D_{eff}^{O_2-H_2O}$ is the effective molecular diffusion coefficient for the O_2-H_2O binary system, $D_{eff}^{H_2-H_2O}$ is the effective molecular diffusion coefficient for the H_2-H_2O binary system and $D_{eff}^{H_2O,K}$ is the effective Knudsen diffusion coefficient for water. The Knudsen diffusivities of H_2 and O_2 in H_2O do not appear in Eqns (38) and (39) as a consequence of the assumption of uniform pressure. Uniform pressure implies zero total molar flux, i.e. equi-molar counter-diffusion. As a result, the Knudsen diffusivity of H_2 in H_2O is the same as that of H_2O in H_2 , i.e. $D_{eff}^{H_2-H_2O,K} = D_{eff}^{H_2O-H_2,K}$, but the fluxes are opposite, so that the corresponding terms cancel. An analogous

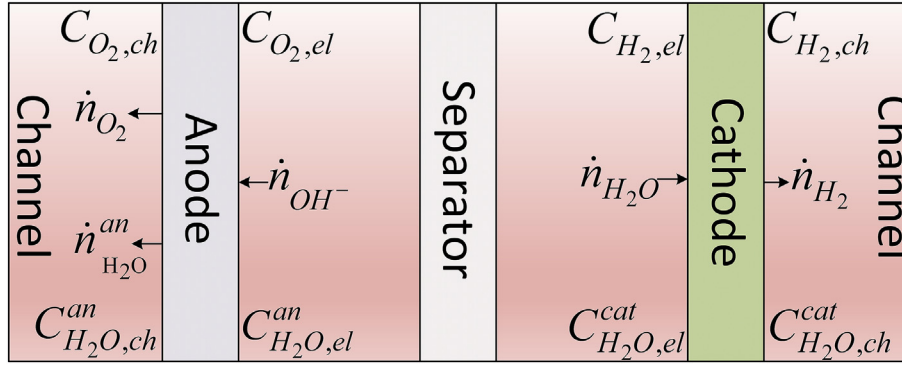


Fig. 2. Species concentrations and molar fluxes inside the alkaline electrolyser cell.

argument applies to O_2 .

The effective Knudsen diffusion can be modelled using kinetic theory [44,45] as follows:

$$D_{eff}^{H_2O,K} = \frac{4}{3} r \sqrt{\frac{8R^*T}{\pi M_{H_2O}}} \quad (40)$$

where r is the mean pore radius and M_{H_2O} is the molar weight of H_2O . Using the Chapman-Enskog theory of the ideal gas, the effective molecular binary diffusion coefficients, $D_{eff}^{O_2-H_2O}$ and $D_{eff}^{H_2-H_2O}$ can be expressed as [44,46]

$$D_{eff}^{O_2-H_2O} = 0.00133 \left(\frac{1}{M_{O_2}} + \frac{1}{M_{H_2O}} \right)^{1/2} \frac{T^{3/2}}{P_{an} \sigma_{O_2-H_2O}^2 \Gamma_D} \quad (41)$$

$$D_{eff}^{H_2-H_2O} = 0.00133 \left(\frac{1}{M_{H_2}} + \frac{1}{M_{H_2O}} \right)^{1/2} \frac{T^{3/2}}{P_{cat} \sigma_{H_2-H_2O}^2 \Gamma_D} \quad (42)$$

where M_{O_2} and M_{H_2} are the molar weights of O_2 and H_2 , $\sigma_{O_2-H_2O}$ and $\sigma_{H_2-H_2O}$ are the mean molecular radii of species O_2-H_2 and H_2-H_2O and Γ_D is a dimensionless diffusion collision integral. Γ_D , $\sigma_{O_2-H_2O}$ and $\sigma_{H_2-H_2O}$ can be expressed analytically as [47]

$$\Gamma_D = \frac{1.06}{\tau^{0.156}} + \frac{0.193}{\exp(0.476\tau)} + \frac{1.036}{\exp(1.53\tau)} + \frac{1.765}{3.894\tau} \quad (43)$$

$$\begin{aligned} \sigma_{O_2-H_2O} &= \frac{\sigma_{O_2} + \sigma_{H_2O}}{2} \\ \sigma_{H_2-H_2O} &= \frac{\sigma_{H_2} + \sigma_{H_2O}}{2} \end{aligned} \quad (44)$$

$$\begin{aligned} \tau_{O_2-H_2O} &= \frac{kT}{\epsilon_{O_2-H_2O}} \\ \tau_{H_2-H_2O} &= \frac{kT}{\epsilon_{H_2-H_2O}} \end{aligned} \quad (45)$$

and the Lennard-Jones energies $\epsilon_{O_2-H_2O}$ and $\epsilon_{H_2-H_2O}$ can be expressed as

$$\begin{aligned} \epsilon_{O_2-H_2O} &= \sqrt{\epsilon_{O_2} \epsilon_{H_2O}} \\ \epsilon_{H_2-H_2O} &= \sqrt{\epsilon_{H_2} \epsilon_{H_2O}} \end{aligned} \quad (46)$$

The values of σ_{O_2} , σ_{H_2} and σ_{H_2O} are 3.467 Å, 2.827 Å and 2.641 Å, respectively [48]. The Lennard-Jones potentials, ϵ_i/k , for O_2 , H_2 and

H_2O are 106.7, 59.7 and 809.1 K, respectively. The values of $D_{eff}^{O_2-H_2O}$ and $D_{eff}^{H_2-H_2O}$ can be obtained by solving Eqs. (38)–(46).

The resulting contribution to the overpotential is

$$V_{con} = \frac{R^*T}{4F} \ln \frac{C_{O_2,el}^{an}}{C_{O_2,0}^{an}} + \frac{R^*T}{2F} \ln \frac{C_{H_2,el}^{cat}}{C_{H_2,0}^{cat}} \quad (47)$$

Here “0” represents a working condition taken as a reference.

2.3.4. Ohmic overpotential

The electrodes, electrolyte and separator are the main contributors to a further overpotential in an alkaline electrolyser cell arising in the resistances of these elements. It is normally assumed that this overpotential is ohmic, that is, linearly proportional to the current:

$$V_{ohm} = IR_{cell} = I(R_e + R_{el} + R_s) \quad (48)$$

where R_{cell} is the effective ohmic resistance of the cell, R_e is the electrode resistance, R_{el} is the electrolyte resistance, including the effects of electrolyte concentration and gas bubbles, and R_s is the separator resistance.

The assumption of ohmic resistance implies that the resistance of each element depends only on the properties of its constituent material(s) and its geometry via

$$R = \rho \frac{l}{A} \quad (49)$$

where the current flows in a path of length l with cross-sectional area A in a material with resistivity ρ . In Eq. (49) l and A correspond literally to physical dimensions only for simple geometries, such as a long conducting bar ($l > \sqrt{A}$) or a thin conducting sheet perpendicular to the plane ($l < \sqrt{A}$), surrounded by insulator, so that edge effects may be safely ignored.

For solid materials with well-defined charge carriers, and for liquid electrolytes in which charge build-up is negligible, representing the conductor by a resistivity which varies only with temperature is well justified. This is true also for the resistances contributing to Eq. (48). The porous natures of the electrodes and separator, and the interruption of the electrolyte conduction path by bubbles, affect the detailed geometry of the element, but not its intrinsic resistivity, ρ_0 . The approach taken to model these resistances is typically to calculate an effective resistivity, ρ_{eff} , incorporating porosity etc., so that the geometric factors in Eq. (49) may be taken as the gross external dimensions of the conductor.

The electrodes, separator and bubble zone are examples of inhomogeneous conductors. Exact theory is intractable for such systems, but many approximate models have been developed to describe the conduction properties of composite conductors consisting of inclusions of conductor 2 in a matrix of conductor 1 in terms of an effective conductivity, an approach generally called homogenisation. At low concentrations of the inclusion phase, most models give essentially the same result, independent of the detailed arrangement or morphology of the inclusions. This is true, for instance, of the much-used Maxwell–Eucken [49] and Bruggeman mean-field [50] models (e.g. Refs. [51–53]). In this approach, which will be followed here, it is assumed that no there is penetration of the electrodes by the liquid electrolyte and that the pores are insulating relative to the electrode material. The same approach is applied to the bubble zone, with the bubbles regarded as insulating relative to the electrolyte itself. Solving Bruggeman's equation for the conductivity of a two-phase conductor with volume fraction ϕ_{incl} of the inclusion phase [50],

$$1 - \phi_{incl} = \left(\frac{\sigma_{incl} - \sigma_{eff}}{\sigma_{incl} - \sigma_{matrix}} \right) \left(\frac{\sigma_{matrix}}{\sigma_{eff}} \right)^{1/3} \quad (50)$$

with the conductivity of the inclusion phase, σ_{incl} , set to zero, gives for the effective conductivity

$$\sigma_{eff} / \sigma_{matrix} = (1 - \phi_{incl})^{3/2} \quad (51)$$

The separator represents the obverse case, that of a percolating network of pores filled with conductor in an insulating matrix. Since at high concentration of the inclusion phase different approaches to homogenisation produce very different effective conductivities, a direct calculational approach based on an assumed microstructure is adopted here.

2.3.4.1. Electrodes. The following equations for the anode also apply to the cathode. The resistance of the anode is

$$R_{an} = \rho_{eff}^{an} \frac{\delta_{an}}{A_e} \quad (52)$$

where ρ_{eff}^{an} is the effective resistivity of the anode. Eq. (51) yields

$$\rho_{eff}^{an} = \frac{\rho_0^{an}}{(1 - \varepsilon_{an})^{3/2}} \quad (53)$$

where ρ_0^{an} is the resistivity of the 100%-dense anode material at reference temperature and ε_{an} is the porosity of the anode.

Introducing κ as the temperature coefficient of resistivity, the anode resistance at any temperature is

$$R_{an} = \frac{\rho_0^{an}}{(1 - \varepsilon_{an})^{3/2}} \frac{\delta_{an}}{A_e} [1 + \kappa_{an}(T - T_{ref})] \quad (54)$$

and likewise for the cathode. The resultant electrode resistance is

2.3.4.2. Electrolyte. To make the problem of bubbles in the electrolyte tractable, the electrolyte may be divided into a bubble-free zone (bf) of width $l_{an-s} - \beta_{an}$ and a bubble zone (bz) of width β_{an} for the anode side of the cell, and similarly for the cathode side, as shown in Fig. 3. Experimentally, it was found that the width of the bubble zone in an electrolysis cell varied from 0.4 to 0.6 mm [54], which is a substantial fraction of the typical electrode–separator distance.

Separating out the contribution from the bubble zone, the total electrolyte resistance for the anode side can be expressed as

$$R_{el}^{an} = R_{bf}^{an} + R_{bz}^{an} = \rho_{el} \frac{l_{an-s} - \beta_{an}}{A_e} + \rho_{bz}^{an} \frac{\beta_{an}}{A_e} \quad (56)$$

where ρ_{el} is the resistivity of the bubble-free electrolyte and ρ_{bz}^{an} is the effective resistivity of the electrolyte in the anode bubble zone. Once again, Bruggeman's model (Eq. (51)) may be employed to obtain the effective resistivity in the anode bubble zone with electrolyte-phase gas bubble volume fraction, sometimes called the void fraction, ϕ_{an} :

$$\rho_{bz}^{an} = \frac{\rho_{el}}{(1 - \phi_{an})^{3/2}} \quad (57)$$

Eq. (57) has been experimentally validated for a surprisingly wide range of conditions (electrode gap, electrolyte flow velocity, current density) [55]. The total electrolyte resistance is then

$$\begin{aligned} R_{el} &= R_{el}^{an} + R_{el}^{cat} \\ &= \frac{\rho_{el,ref}}{[1 + \kappa_{el}(T - T_{ref})]} \times \left[\frac{l_{an-s} - \beta_{an}}{A_e} + \frac{1}{(1 - \phi_{an})^{3/2}} \frac{\beta_{an}}{A_e} \right. \\ &\quad \left. + \frac{l_{cat-s} - \beta_{cat}}{A_e} + \frac{1}{(1 - \phi_{cat})^{3/2}} \frac{\beta_{cat}}{A_e} \right] \end{aligned} \quad (58)$$

In Appendix A it is shown that, subject to usual assumptions, in the steady state the surface bubble fraction at the electrode and the volume fraction in the bubble zone are in fact the same, $\phi = \Theta$.

2.3.4.3. Separator. The separator must provide a continuous ionic conduction path while blocking gas mixing, achieved by pores extending through the structure. The volume fraction of these pores is the porosity, ε_s , and their effective length relative to the thickness of the separator is given by the tortuosity,

$$\tau_s = \frac{l_{eff}}{\delta_s} \quad (59)$$

The ratio of the volume of electrolyte absorbed inside the pores to the total pore volume defines the wettability factor of the separator for the electrolyte, ω_s [13]. The effective porosity is then $\omega_s \varepsilon_s$. Assuming a uniform current distribution across A_s , the external cross-sectional area of the separator, the pores constitute an equivalent conductor with area equal to the total cross-sectional area of pores, given by $(\omega_s \varepsilon_s / \tau_s) A_s$, and length $\tau_s \delta_s$. Eq. (49) then gives for the resistance of the separator

$$R_e = R_{an} + R_{cat} = \frac{\rho_0^{an}}{(1 - \varepsilon_{an})^{3/2}} \frac{\delta_{an}}{A_e} [1 + \kappa_{an}(T - T_{ref})] + \frac{\rho_0^{cat}}{(1 - \varepsilon_{cat})^{3/2}} \frac{\delta_{cat}}{A_e} [1 + \kappa_{cat}(T - T_{ref})] \quad (55)$$

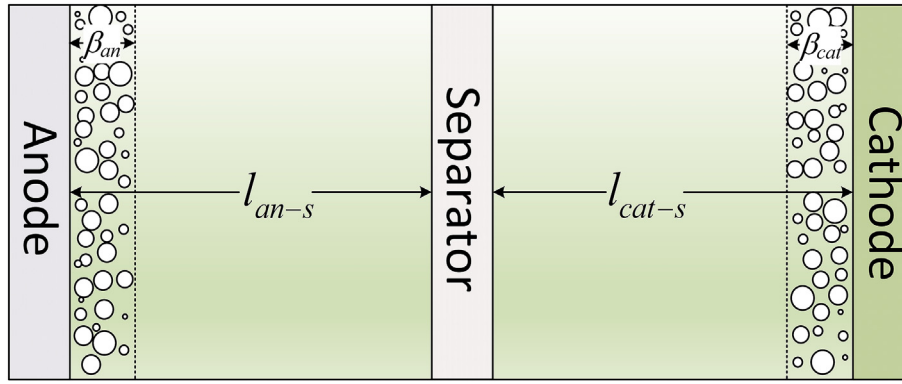


Fig. 3. Electrolyte zones.

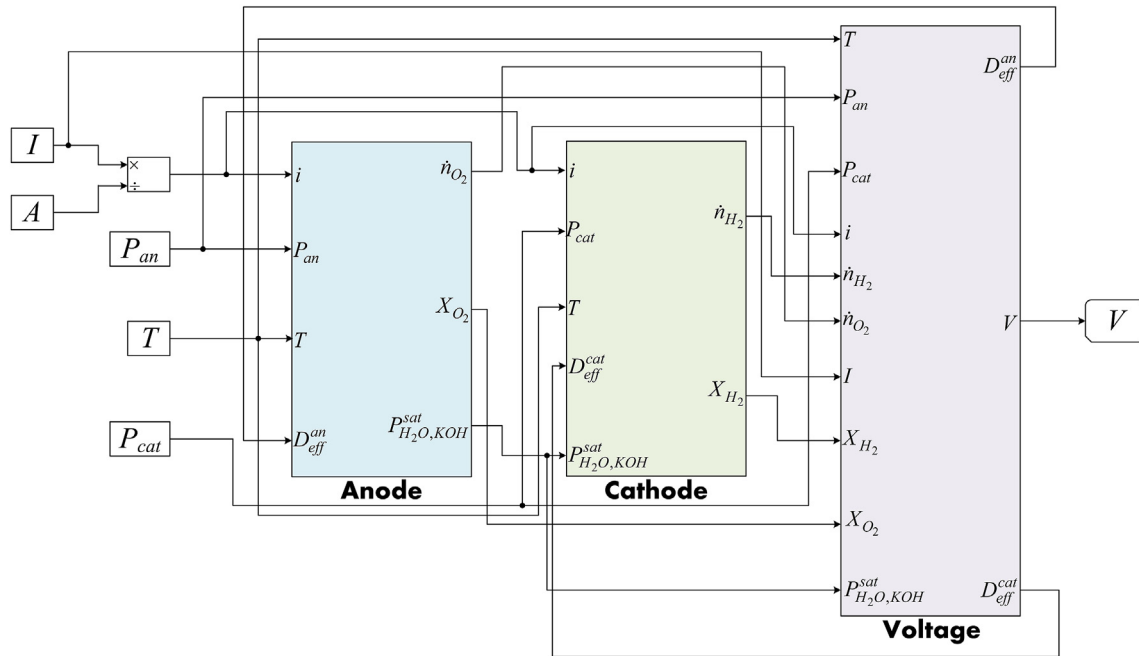


Fig. 4. Simulink model of the alkaline electrolyser cell.

$$R_s = \rho_{el} \frac{\tau_s^2 \delta_s}{\omega_s \varepsilon_s A_s} \quad (60)$$

3. Results and discussion

Fig. 4, which depicts the full Simulink model of the alkaline electrolyser cell, shows how each of the three ancillaries discussed in the previous section contributes to the simulation, and maps the interactions between them. The calculated polarisation curve embodies cell geometry, cell temperature, partial pressures of the gases, bubble coverage on the electrode surfaces and internal parameters such as porosity and tortuosity of the electrodes, electrolyte concentration, separator thickness, active surface area of the electrodes etc.

3.1. Model validation

The model was validated using the sets of experimental

polarisation curves for HRI and PHOEBUS electrolyser reported by several authors [11,27,56,57]. Temperature and pressure effects were explored in the ranges 35–80 °C and 1–9 bar. Seven model parameters ($\gamma_{M,an}$, $\gamma_{M,cat}$, ω , $i_{0,ref}^{an}$, $i_{0,ref}^{cat}$, α_{an} , α_{cat}) whose values could

Table 1
Fixed parameters.

Parameter	Value		Ref.
	HRI electrolyser	PHOEBUS electrolyser	
A_e	300 cm ²	2500 cm ²	[27]
$l_{an/cat-s}$	0.125 cm	0	[27]
δ_e	0.2 cm	0.2 cm	[27]
τ_e	3.65	4.25	[27]
$\Delta G_{c,an}$, $\Delta G_{c,cat}$	80, 51 kJmol ⁻¹	52, 18 kJmol ⁻¹	[61,67,68]
ε_e	0.3	0.41	[27]
A_s	300 cm ²	2500 cm ²	[27]
$\beta_{an/cat}$	0.045 cm	0.045 cm	[54]
δ_s	0.05 cm	0.05 cm	[27]
ε_s	0.42	0.42	[69]
τ_s	2.18	2.18	[69]

Table 2
Fitted parameters.

Parameter	Value	
	HRI electrolyser	PHOEBUS electrolyser
$\gamma_{M,an}$	1.25	2.5
$\gamma_{M,cat}$	1.05	1.5
ω	0.85	0.87
$i_{0,ref}^{an}$	$1 \times 10^{-11} \text{ Acm}^{-2}$	$1 \times 10^{-9} \text{ Acm}^{-2}$
$i_{0,ref}^{cat}$	$1 \times 10^{-3} \text{ Acm}^{-2}$	$1 \times 10^{-3} \text{ Acm}^{-2}$
α_{an}	1.65	1.85
α_{cat}	0.73	0.85

not be reliably estimated were allowed to vary freely. Table 1 lists the values adopted from Ref. [27] for the fixed parameters. Some parameters ($\beta_{an/cat}$, δ_s , ε_s , τ_s) were assumed to be the same for the bubble zone and separator in each electrolyser. Table 2 lists the fitted parameters. Fig. 5 (a, b) compares the fitted polarisation curves and the experimental data from the above publications in a range of temperatures and pressures. The model described here clearly fits the experimental data very well for a wide range of operating conditions. Fig. 5(c) compares the new model and two published models to experimental data for the PHOEBUS electrolyser under standard conditions. The new model provides an improved fit.

The roughness factor (γ_M) depends on the structure of the electrode surface and can be determined experimentally or estimated from electrocatalyst loading, catalyst particle density and size. The roughness factor generally increases as the thickness of the samples increases. In the HRI electrolyser, Ni electrocatalyst on Ni plate is used for the anode (OER) and cathode (HER). In the PHOEBUS electrolyser, Ni/Co₃O₄/Fe electrocatalyst on Ni plate is used for the anode and C-Pt electrocatalyst on Ni plate for cathode. Gira *et al.* [58] determined the roughness factor of the Ni electrocatalyst using AFM topographic measurements and the values of γ_M obtained ranged from 1.05 to 1.4. Singh *et al.* [59] used the methods of spray pyrolysis and sequential solution coating to measure the roughness factor of Co₃O₄ electrocatalyst on Ni plates for the OER and based on oxide loading the values ranged from 1 to 500. Singh *et al.* [60] showed that Ni/Fe oxide electrocatalysts are highly active for the OER in alkaline solutions, but they have very low electrochemically active areas, with relative oxide roughness factors <2. Durst *et al.* [61] used a rotating disc electrode (RDE) method to measure the roughness factor of C-Pt electrocatalyst for the HER and found $\gamma_M \approx 2$. The fitted values produced by the present model of $\gamma_{M,an} = 1.25$ and $\gamma_{M,cat} = 1.05$ for the HRI electrolyser, and $\gamma_{M,an} = 2.5$ and $\gamma_{M,cat} = 1.5$ for the PHOEBUS electrolyser are in this range. Wettability (ω_s) was treated as a fitted parameter because reliable values could not be found in the literature. Values for the charge transfer coefficients for anodes and cathodes are reported to be in the range 0–2 and 0–1 respectively [62]. The fitted values lie within these ranges. For Ni-based electrodes, the exchange current densities for the oxygen reduction and hydrogen oxidation reactions are reported as 10^{-7} – 10^{-12} and 10^{-4} – $10^{-1} \text{ A cm}^{-2}$ [3,63], respectively. The fitted values lie within these ranges. It is anticipated that the values of parameters obtained from a well-validated physically based model may be more reliable than those estimated from indirect experiments with many assumptions and uncertainties.

3.2. Model exploration

Fig. 6 shows the contribution of each source of overpotential to the polarisation curve of the HRI alkaline electrolyser cell at

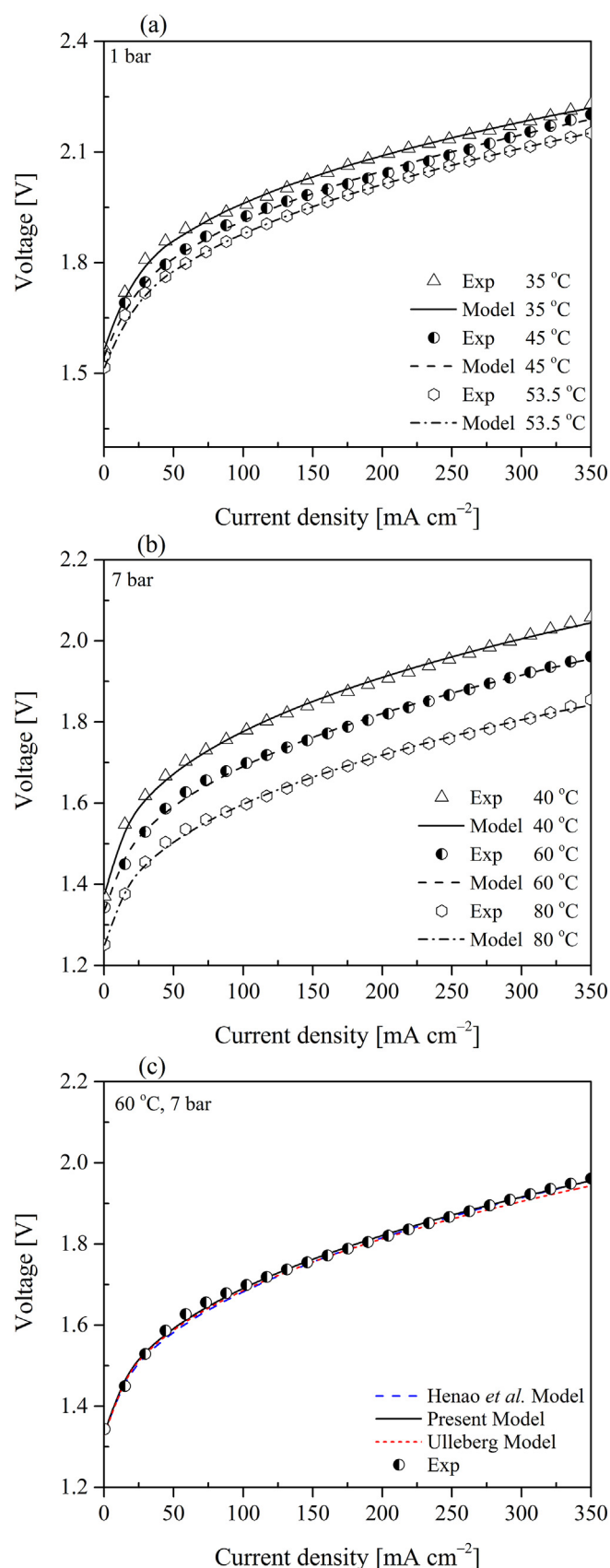


Fig. 5. Comparison between experimental data and model predictions in a range of operating temperatures at constant pressure for (a) the HRI electrolyser [56], (b) the PHOEBUS electrolyser [11,57], (c) comparison between published models [11,27] and the present model based on experimental data for the PHOEBUS electrolyser.

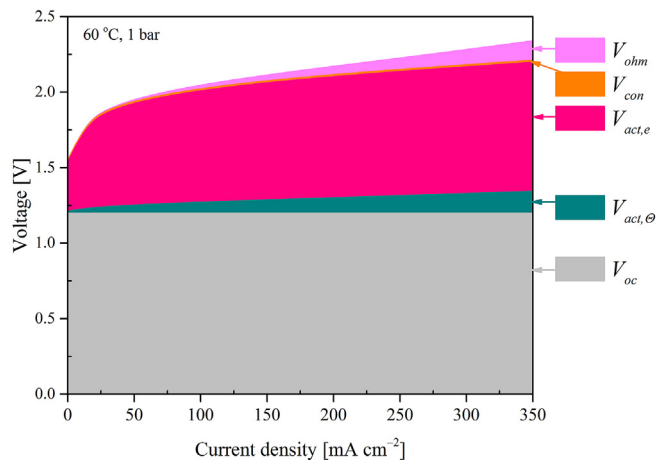


Fig. 6. Contributions of overpotential terms to the polarisation curve. $V_{act,\Theta}$ is the contribution from bubble coverage of the electrodes, while $V_{act,e}$ is the contribution from the bubble-free electrodes.

constant pressure (1 bar) and temperature (60 °C). The concentration (diffusion) overpotential is negligible in the case modelled. The ohmic contribution is relatively small in total and within that, the contribution from the electrodes ($<10^{-9} \Omega$) is very small and that from the electrolyte (0.001 Ω) is smaller than the separator contribution ($\sim 0.002 \Omega$). The contribution to the activation overpotential from bubble coverage of the electrodes is not negligible. Strategies to lessen the bubble coverage without introducing excessive parasitic power consumption may have a benefit in higher efficiency. The dominant contribution remains the activation overpotential of the bubble-free electrodes, with the majority coming from the anode owing to its relatively small exchange current density.

Fig. 7 explores the influence of operating temperature on the electrode bubble coverage (Θ) and its contribution to the activation overpotential of the HRI electrolyser. The contribution is relatively small, but the advantage of operating at elevated temperature to promote the detachment of bubbles from the electrode surfaces is clear.

Fig. 8 explores the effect of the electrode exchange current densities on the activation overpotential curve of the HRI electrolyser. The cathode activation overpotential is relatively small due to

the fast kinetics of the hydrogen evolution reaction, apparent in the relatively high fitted value of the cathode exchange current density. The cell overpotential is dominated by the anode activation overpotential because of the slow kinetics of the oxygen evolution reaction (OER). In order to obtain higher anode exchange current density, research effort should be directed to developing new catalysts and optimising the electrode structural parameters. Procedures to select oxide electrocatalysts for OER have been published [64,65].

Despite the higher anode activation overpotential, the scope for lowering the total overpotential by improving the cathode is significant, as seen from the greater sensitivity of overpotential to the same logarithmic change in exchange current density in **Fig. 8(b)** compared to **Fig. 8(a)**. This point is discussed in detail with reference to the PEM electrolyser in Ref. [15].

Fig. 9 explores the effect of electrode roughness factor on the polarisation curve of the HRI electrolyser. Generally speaking, higher roughness helps to increase the exchange current density, with the same effect as making the reaction kinetics faster, thus lowering the overpotentials. On the other hand, roughening the electrode surface (through oxide loading) may result in higher rather than lower overpotentials, because gas bubbles may be trapped within surface irregularities, blocking access to the electrocatalyst. **Fig. 9** suggests that moderate roughening of the electrocatalyst surface is slightly beneficial, especially at the cathode.

Fig. 10 explores the effect of the electrode charge transfer coefficient on the polarisation curve of the HRI electrolyser. Relative to the fitted values of $\alpha_{an} = 1.75$ and $\alpha_{cat} = 0.8$, the polarisation curve is more sensitive to improvements in α_{an} .

Fig. 11 explores the influence of separator wettability factor on the polarisation curve and the contributions of wettability factor to the separator resistance at elevated temperatures for the HRI electrolyser at 1 bar pressure. Wettability below 0.3 is extremely undesirable, especially when combined with low operating temperature.

Fig. 12 explores the influence of the bubble volume fraction on the electrolyte resistance at elevated temperatures and pressures for the HRI electrolyser. The contribution of the bubble zones to ohmic losses is relatively small and, as expected, minimised by increasing the operating temperature and pressure.

Fig. 13 explores the effects of temperature and pressure on the cell polarisation curve for the HRI electrolyser. At constant temperature (**Fig. 13(a)**), the effect of increasing pressure is to increase

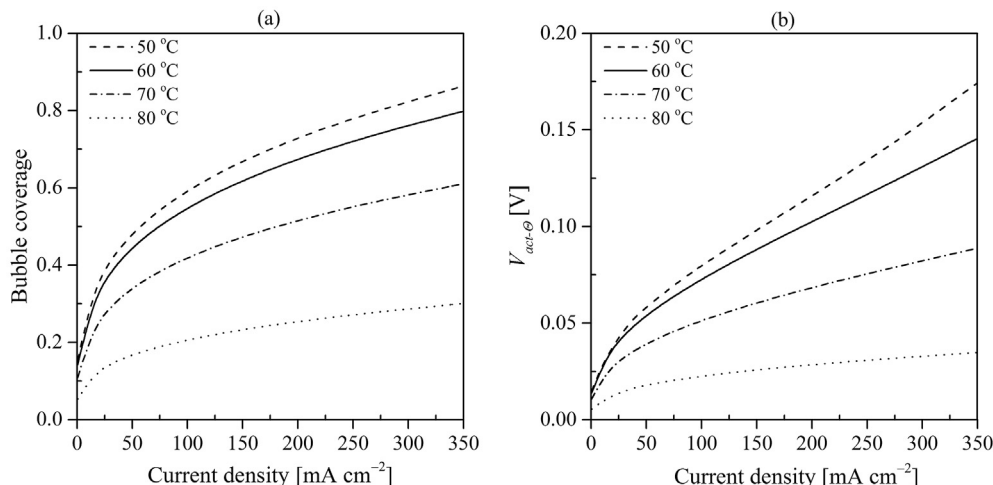


Fig. 7. Relationship between electrode bubble coverage (Θ) and activation overpotential in a range of operating temperatures.

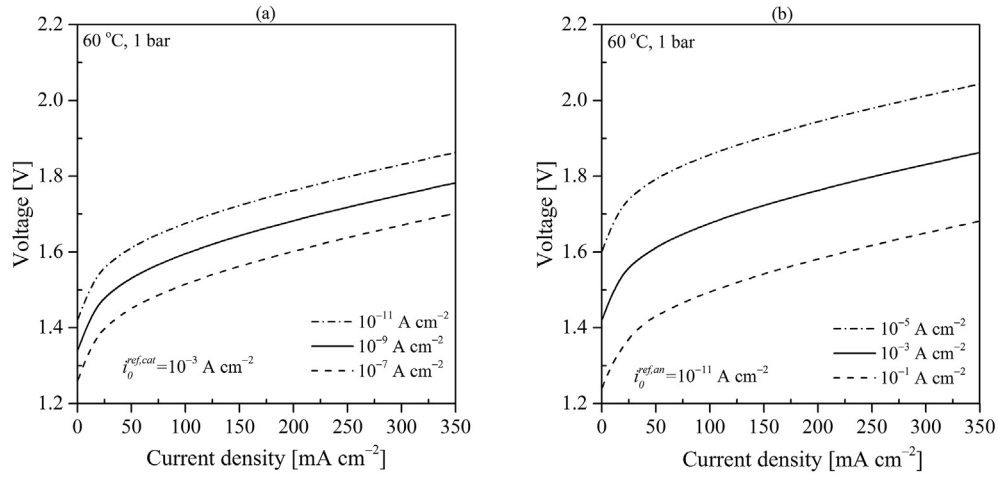


Fig. 8. Effect of electrode exchange current densities on the polarisation curve: (a) anode and (b) cathode.

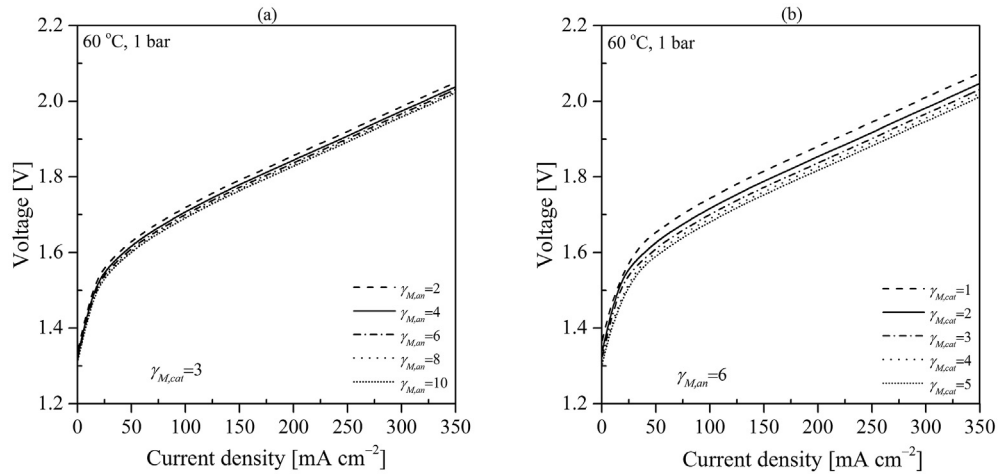


Fig. 9. Effect of electrode roughness factor (γ_M) on the polarisation curve: (a) anode and (b) cathode.

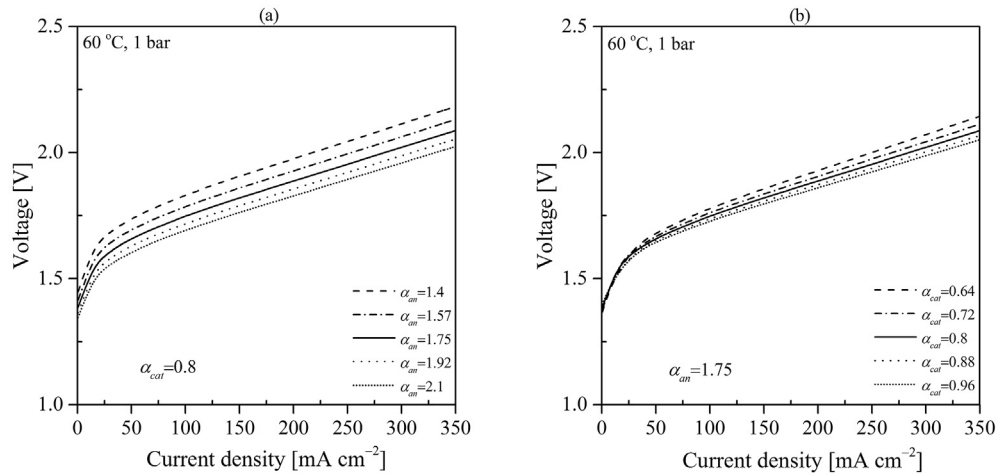


Fig. 10. Effect of electrode charge transfer coefficient ($\alpha_{an/cat}$) on the polarisation curve: (a) anode and (b) cathode for increments of $\pm 10\%$ and $\pm 20\%$ relative to the fitted values.

the cell voltage non-linearly via the open-circuit voltage (Eq (23)). At constant pressure (Fig. 13(b)), increasing the operating temperature significantly lowers the cell voltage owing to higher rates of

reaction and the higher conductivity of the electrolyte and separator. The diminishing extra loss at higher pressures may make high-pressure electrolyser operation attractive in circumstances

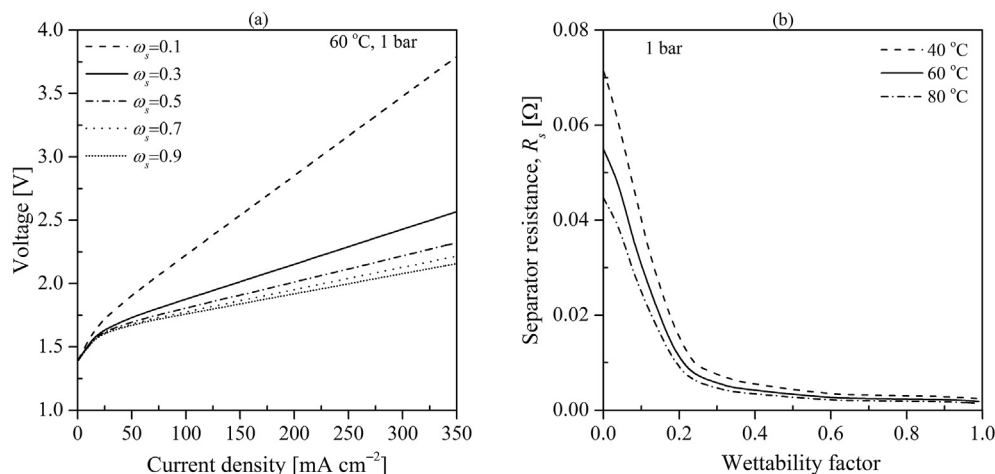


Fig. 11. Effect of separator wettability factor (ω_s) on (a) the polarisation curve at constant temperature and pressure, and (b) on separator resistance in a range of operating temperatures.

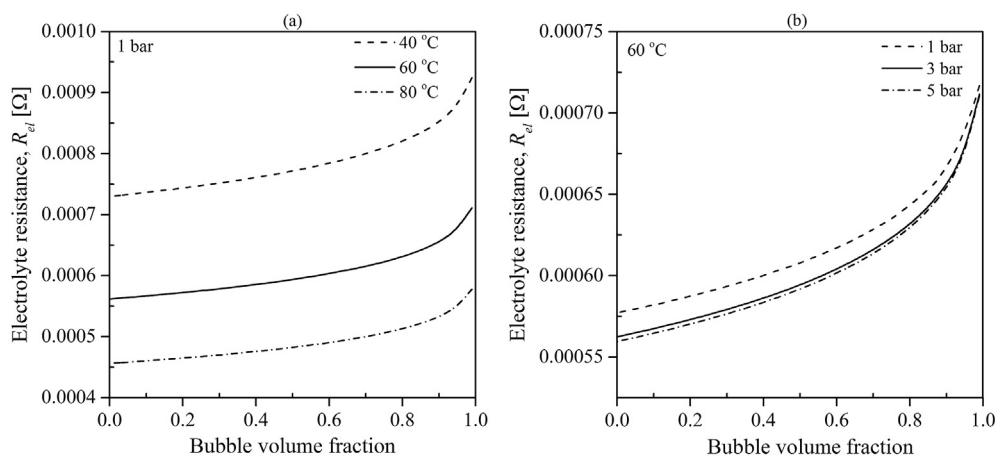


Fig. 12. Effect of bubble volume fraction (ϕ) on electrolyte resistance in (a) a range of operating temperatures and (b) a range of operating pressures.

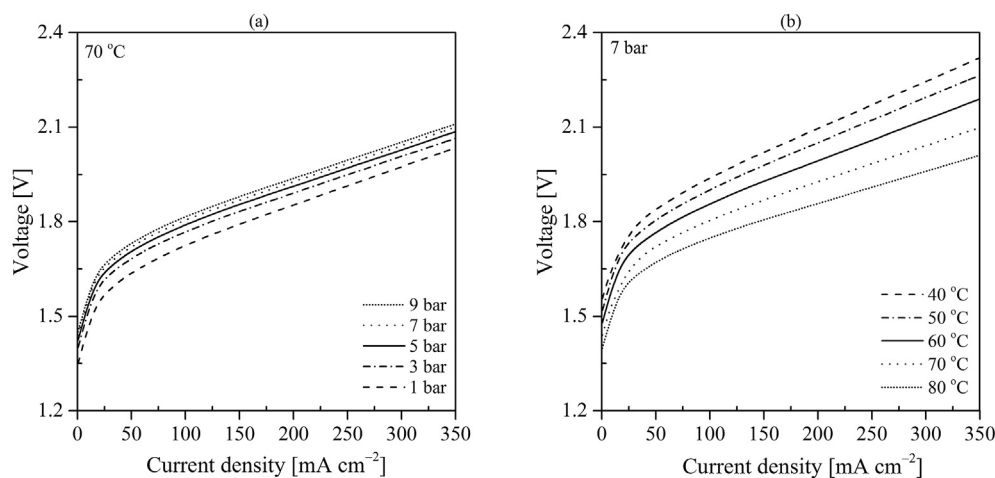


Fig. 13. Effect of different operating (a) pressures at 70 °C and (b) temperatures at 7 bar on the polarisation curve.

where a separate compressor would be required to compress hydrogen delivered at 1 atm.

4. Summary and conclusions

A new model of an alkaline electrolyser cell has been developed based on modules incorporating the physical characteristics of the anode, cathode, electrolyte and separator. Through this model, the cell polarisation curve may be related to the physical characteristics of the cell components. The model is structured so that it can be easily extended to a stack of electrolyser cells. Ultimately, this model will be incorporated with compatible models of the other components of a hydrogen-based energy system to form a whole-of-system model that can be used to simulate the system behaviour under off-grid conditions.

The simulation was tested against published experimental data and fitted very well, with seven free model parameters (wettability factor, charge transfer coefficients, roughness factors and reference exchange current densities) related to physical parameters whose values are difficult to estimate reliably. When fitted to the same experimental data used to test published models, the new model provided a slightly better fit. Thus the approach of using a simplified 1D model has been demonstrated to have good functionality. This also demonstrates that an empirical approach, while convenient, is largely unnecessary.

In addition to predicting the cell performance for specified parameter values, the simulation provides a useful tool for investigating the sensitivity of the polarisation curve of a given electrolyser to improvements in selected parameters. By displaying the cell voltage as the sum of its components, the model showed how the exchange current densities of the anode and cathode influence the polarisation curve (via their activation overpotentials). A higher anode exchange current density, achieved through improved electrocatalysts, promises significantly improved efficiency when operating at high cell current density. On the other hand, several orders of magnitude increase in the small anode exchange current density of the modelled electrolyser cell would be needed to have a substantial impact on the anode activation overpotential.

Because the model relates alkaline electrolyser cell performance to fundamental physical parameters, it may be useful in developing improved electrodes, electrocatalysts and bubble management. The model is able to be extended by incorporating the characteristics of new materials into the relevant ancillaries, for example conventional composite versus novel electrode microstructures. A major challenge is to develop a physically-based model to calculate the bubble coverage on the electrode surface and the bubble void fractions in the bubble zones.

Acknowledgement

ZA acknowledges receipt of a postgraduate scholarship from Griffith University.

Appendix A: Equivalence of surface and volume bubble fractions

Consider a volume of electrolyte with cross-sectional area A and thickness t in the z direction, bounded at one face by an electrode of area A . Inserting an imaginary plane at z , and denoting the total cross-sectional area of bubbles intersecting this plane as $a(z)$, the total volume of bubbles is

$$V = \int_0^t a(z) dz = \bar{a} t \quad (\text{A.1})$$

where \bar{a} is the average total cross-sectional area. Supposing that there are on average N_V bubbles per unit volume with average volume \bar{v} , the total bubble volume may be written as $N_V \cdot A \cdot \bar{v}$, giving for the average volume fraction

$$\phi = N_V \bar{v} \quad (\text{A.2})$$

In a slice of thickness dz the volume of bubbles is $N_V \cdot A \cdot dz \cdot \bar{v}$, so $dV/dz = N_V A \bar{v}$. From Eq. (A.1) this is just \bar{a} , so the average cross-sectional area fraction can be obtained as

$$\Theta = \frac{\bar{a}}{A} = N_V \bar{v} \quad (\text{A.3})$$

and comparing Eqs. (A.2) and (A.3) it is found that the average volume and area fractions within the bubble zone are the same, as intuition suggests. If the imaginary plane is displaced to the electrode surface and it is assumed, as usual, that the bubbles are truncated spheres, then the same result applies at the electrode, and the average bubble volume fractions ϕ in Eq. (58) are the same as the average bubble coverage fractions on the electrodes, Θ in Eq. (31).

The argument above assumes that the bubbles are stationary, but in the steady state the rate of increase of bubble volume through generation at the electrode in the zone under consideration is by definition the same as the rate of removal on average. Therefore, as long as the current changes slowly compared to the transit time of a bubble through the bubble zone, the argument remains sound.

Now supposing that the electrolyte and bubbles are moving in the same direction at velocities u_{el} and u_b respectively, the bubble volume fraction in an otherwise homogeneous fluid can be expressed as [66]

$$\phi = \frac{1}{1 + S \left(\frac{1-x}{x} \right) \left(\frac{\rho_b}{\rho_{el}} \right)} \quad (\text{A.4})$$

where $S = u_{el}/u_b$ is the slip or velocity ratio, ρ_{el} and ρ_b are the densities of the electrolyte and gas respectively, and $x = \dot{m}_g/(\dot{m}_g + \dot{m}_{el})$ is the dryness factor. With no further assumptions, Eq. (A.4) yields

$$\phi = \frac{1}{1 + \frac{\dot{v}_{el}/u_{el}}{\dot{v}_b/u_b}} \quad (\text{A.5})$$

where \dot{v}_{el} and \dot{v}_b are the volumetric flow rates of the electrolyte and bubbles respectively. Considering for convenience a cylindrical element of electrolyte with area a_{el} perpendicular to the flow direction, for that element $\dot{v}_{el}/u_{el} = a_{el}$ and likewise for an element of gas. Assuming that the flow is laminar, the same result applies to all elements of the electrolyte collected into a single volume element and likewise for the gas. The ratio of the total cross-sectional area of electrolyte to that of bubbles is then a_{el}/a_b and Eq. (A.5) yields $\phi = a_b/a_{el} = \Theta$, showing that the equivalence of the volume fraction of bubbles to the surface fraction is in fact general as long as the two-phase flow is laminar.

References

- [1] Department of Energy USA. Report of the hydrogen production expert panel.

- 2013.
- [2] Ludwig-Bölkow-Systemtechnik GmbH. Accessed via www.H2stations.org.
- [3] Zeng Kai, Zhang Dongke. Recent progress in alkaline water electrolysis for hydrogen production and applications. *Prog Energy Combust Sci* 2010;36(3): 307–26.
- [4] Barton John, Gammon Rupert. The production of hydrogen fuel from renewable sources and its role in grid operations. *J Power Sources* 2010;195(24): 8222–35.
- [5] Ursula Alfredo, Gandia Luis M, Sanchis Pablo. Hydrogen production from water electrolysis: current status and future trends. *Proc IEEE* 2012;100(2):410–26.
- [6] Ekman Claus Krog, Jensen Søren Højgaard. Prospects for large scale electricity storage in Denmark. *Energy Convers Manag* 2010;51(6):1140–7.
- [7] Kiaee Mahdi, Cruden Andrew, Chladek Petr, Infield David. Demonstration of the operation and performance of a pressurised alkaline electrolyser operating in the hydrogen fuelling station in Porsgrunn, Norway. *Energy Convers Manag* 2015;94:40–50.
- [8] Zhang Linfeng, Xiang Jing. The performance of a grid-tied microgrid with hydrogen storage and a hydrogen fuel cell stack. *Energy Convers Manag* 2014;87:421–7.
- [9] Khalilnejad A, Riahy GH. A hybrid wind-PV system performance investigation for the purpose of maximum hydrogen production and storage using advanced alkaline electrolyzer. *Energy Convers Manag* 2014;80:398–406.
- [10] Paidar M, Fateev V, Bouzek K. Membrane electrolysis—history, current status and perspective. *Electrochim Acta* 2016;209:737–56.
- [11] Ulleberg Øystein. Modeling of advanced alkaline electrolyzers: a system simulation approach. *Int J Hydrogen Energy* 2003;28(1):21–33.
- [12] Pletcher Derek, Walsh Frank C. *Industrial electrochemistry*. Springer Science & Business Media; 2012.
- [13] Vermeiren PH, Leysen R, Beckers H, Moreels JP, Claes A. The influence of manufacturing parameters on the properties of macroporous Zirfon® separators. *J Porous Mater* 2008;15(3):259–64.
- [14] Abidin Z, Webb CJ, Gray EMacA. Solar hydrogen hybrid energy systems for off-grid electricity supply: a critical review. *Renew Sustain Energy Rev* 2015;52: 1791–808.
- [15] Abidin Z, Webb CJ, Gray EMacA. Modelling and simulation of a proton exchange membrane (PEM) electrolyser cell. *Int J Hydrogen Energy* 2015;40(39):13243–57.
- [16] Abidin Z, Webb CJ, Gray EMacA. PEM fuel cell model and simulation in Matlab—Simulink based on physical parameters. *Energy* 2016;116:1131–44.
- [17] Olateju Babatunde, Kumar Amit. A techno-economic assessment of hydrogen production from hydropower in Western Canada for the upgrading of bitumen from oil sands. *Energy* 2016;115:604–14.
- [18] El-Askary WA, Sakr IM, Ibrahim KA, Balabel A. Hydrodynamics characteristics of hydrogen evolution process through electrolysis: numerical and experimental studies. *Energy* 2015;90:722–37.
- [19] Hug W, Bussmann H, Brinner A. Intermittent operation and operation modeling of an alkaline electrolyzer. *Int J hydrogen energy* 1993;18(12): 973–7.
- [20] Griesshaber W, Sick F. Simulation of hydrogen-oxygen—systems with pv for the self-sufficient solar house. Freiburg im Breisgau: FhG-ISE; 1991.
- [21] Ulleberg Ø, Mørner SO. TRNSYS simulation models for solar-hydrogen systems. *Sol Energy* 1997;59(4):271–9.
- [22] Meurer C, Barthels H, Brocke WA, Emonts B, Groehn HG. PHOEBUS—an autonomous supply system with renewable energy: six years of operational experience and advanced concepts. *Sol energy* 1999;67(1):131–8.
- [23] Gutiérrez-Martín F, García-De María JM, Bañri A, Laraqi N. Management strategies for surplus electricity loads using electrolytic hydrogen. *Int J Hydrogen Energy* 2009;34(20):8468–75.
- [24] Takahashi Rion, Hirota Kinoshta, Toshiaki Murata, Junji Tamura, Masatoshi Sugimasa, Akiyoshi Komura, et al. Output power smoothing and hydrogen production by using variable speed wind generators. *Ind Electron IEEE Trans* 2010;57(2):485–93.
- [25] K Havre, Borg P, Tommerberg K. Modeling and control of pressurized electrolyzer for operation in stand alone power systems. Conference Modeling and control of pressurized electrolyzer for operation in stand alone power systems. p. 63–78.
- [26] Hammoudi M, Henao C, Agbossou K, Dubé Y, Doumbia ML. New multi-physics approach for modelling and design of alkaline electrolyzers. *Int J Hydrogen Energy* 2012;37(19):13895–913.
- [27] Henao Christian, Agbossou Kodjo, Hammoudi Mhamed, Dubé Yves, Cardenas Alben. Simulation tool based on a physics model and an electrical analogy for an alkaline electrolyzer. *J Power Sources* 2014;250:58–67.
- [28] Bergen A, Pitt L, Rowe A, Wild P, Djilali N. Transient electrolyser response in a renewable-regenerative energy system. *Int J Hydrogen Energy* 2009;34(1): 64–70.
- [29] Vogt H, Balzer RJ. The bubble coverage of gas-evolving electrodes in stagnant electrolytes. *Electrochim Acta* 2005;50(10):2073–9.
- [30] Krishna R, Wesselingh JA. The Maxwell-Stefan approach to mass transfer. *Chem Eng Sci* 1997;52(6):861–911.
- [31] Wang Caisheng, Hashem Nehrir M, Shaw Steven R. Dynamic models and model validation for PEM fuel cells using electrical circuits. *IEEE Trans Energy Convers* 2005;20(2):442–51.
- [32] Balej J. Water vapour partial pressures and water activities in potassium and sodium hydroxide solutions over wide concentration and temperature ranges. *Int J Hydrogen Energy* 1985;10(4):233–43.
- [33] LeRoy Rodney L, Bowen Christopher T, LeRoy Donald J. The thermodynamics of aqueous water electrolysis. *J Electrochem Soc* 1980;127(9):1954–62.
- [34] Bard Allen J, Faulkner Larry R. *Fundamentals and applications. Electrochemical methods*. second ed. New York: Wiley; 2001.
- [35] Rossmel Jan, Logadottir Ashildur, Nørskov Jens Kehlet. Electrolysis of water on (oxidized) metal surfaces. *Chem Phys* 2005;319(1):178–84.
- [36] Kim Seongyul, Koratkar Nikhil, Karabacak Tansel, Lu Toh-Ming. Water electrolysis activated by Ru nanorod array electrodes. *Appl Phys Lett* 2006;88(26): 263106.
- [37] Amphlett John C, Baumert RM, Mann Ronald F, Peppley Brant A, Roberge Pierre R, Harris Thomas J. Performance modeling of the Ballard Mark IV solid polymer electrolyte fuel cell I. Mechanistic model development. *J Electrochem Soc* 1995;142(1):1–8.
- [38] Larminie James, Dicks Andrew, McDonald Maurice S. *Fuel cell systems explained*. Chichester, UK: J. Wiley; 2003.
- [39] Thampan Tony, Malhotra Sanjiv, Zhang Jingxin, Datta Ravindra. PEM fuel cell as a membrane reactor. *Catal Today* 2001;67(1):15–32.
- [40] Atkins Peter William. *The elements of physical chemistry*. Oxford University Press Oxford United Kingdom; 1992.
- [41] Hammoudi M, Henao C, Agbossou K, Dubé Y, Doumbia ML. New multi-physics approach for modelling and design of alkaline electrolyzers. *Int J Hydrogen Energy* 2012;37(19):13895–913.
- [42] Piontelli R, Mazza B, Pedeferri P, Tognoni A. Ricerche sullo sviluppo elettrochimico di gas e sugli effetti anomali che lo accompagnano. Sviluppo da soluzione acquosa. *Electrochim Metall* 1967;2:257–87.
- [43] Ni Meng, Leung Michael KH, Leung Dennis YC. A modeling study on concentration overpotentials of a reversible solid oxide fuel cell. *J Power Sources* 2006;163(1):460–6.
- [44] Hernández-Pacheco Eduardo, Singh Devinder, Hutton Phillip N, Patel Nikhil, Mann Michael D. A macro-level model for determining the performance characteristics of solid oxide fuel cells. *J Power Sources* 2004;138(1):174–86.
- [45] Zhu Huayang, Kee Robert J. A general mathematical model for analyzing the performance of fuel-cell membrane-electrode assemblies. *J Power Sources* 2003;117(1):61–74.
- [46] Reid Robert C, Prausnitz John M, Poling Bruce E. *The properties of gases and liquids*. 1987.
- [47] Chu Liang-Yin, Park Sang-Hoon, Yamaguchi Takeo, Nakao Shin-ichi. Preparation of thermo-responsive core-shell microcapsules with a porous membrane and poly(N-isopropylacrylamide) gates. *J Membr Sci* 2001;192(1–2): 27–39.
- [48] Ni Meng, Leung Michael KH, Leung Dennis YC. An electrochemical model of a solid oxide steam electrolyzer for hydrogen production. *Chem Eng Technol* 2006;29(5):636–42.
- [49] Eucken A. Allgemeine gesetzmäßigkeiten für das wärmeleitvermögen verschiedener stoffarten und aggregatzustände. *Forsch Geb Ingenieurwes A* 1940;11(1):6–20.
- [50] Bruggeman DAG. Dielectric constant and conductivity of mixtures of isotropic materials. *Ann Phys (Leipzig)* 1935;24:636–79.
- [51] Tobias CW. The influence of attached bubbles on potential drop and current distribution at gas-evolving electrodes. *J Electrochem Soc* 1959;134(2).
- [52] Dukovic John, Tobias Charles W. The influence of attached bubbles on potential drop and current distribution at gas-evolving electrodes. *J Electrochem Soc* 1987;134(2):331–43.
- [53] DeLaRue RE, Tobias Charles W. On the conductivity of dispersions. *J Electrochem Soc* 1959;106(9):827–33.
- [54] Perron AL, Kiss LI, Poncsak S. Mathematical model to evaluate the ohmic resistance caused by the presence of a large number of bubbles in Hall-Héroult cells. *J Appl Electrochem* 2007;37(3):303–10.
- [55] Hine Fumio, Murakami Koichi. Bubble effects on the solution IR drop in a vertical electrolyzer under free and forced convection. *J Electrochem Soc* 1980;127(2):292–7.
- [56] Agbossou Kodjo, Mohan Lal Kolhe, Hamelin Jean, Bernier Étienne, Bose Tapan K. Electrolytic hydrogen based renewable energy system with oxygen recovery and re-utilization. *Renew Energy* 2004;29(8):1305–18.
- [57] Barthels H, Brocke WA, Bonhoff K, Groehn HG, Heuts G, Lennartz M, et al. Phoebus-Jülich: an autonomous energy supply system comprising photovoltaics, electrolytic hydrogen, fuel cell. *Int J Hydrogen Energy* 1998;23(4): 295–301.
- [58] J Gira Matthew, Tkacz Kevin P, Hampton Jennifer R. Physical and electrochemical area determination of electrodeposited Ni, Co, and NiCo thin films. 2015. arXiv preprint arXiv:150801778.
- [59] Singh SP, Samuel S, Tiwari SK, Singh RN. Preparation of thin Co₃O₄ films on Ni and their electrocatalytic surface properties towards oxygen evolution. *Int J Hydrogen Energy* 1996;21(3):171–8.
- [60] Singh RN, Singh JP, Singh A. Electrocatalytic properties of new spinel-type MMoO₄ (M = Fe, Co and Ni) electrodes for oxygen evolution in alkaline solutions. *Int J Hydrogen Energy* 2008;33(16):4260–4.
- [61] Durst Julien, Christoph Simon, Hasché Frédéric, Gasteiger Hubert A. Hydrogen oxidation and evolution reaction kinetics on carbon supported Pt, Ir, Rh, and Pd electrocatalysts in acidic media. *J Electrochem Soc* 2015;162(1):F190–203.
- [62] Wendt H, Plzak V. Electrocatalytic and thermal activation of anodic oxygen- and cathodic hydrogen-evolution in alkaline water electrolysis. *Electrochim Acta* 1983;28(1):27–34.
- [63] Hofmann H, Luft G, Wendt H. Advanced alkaline water electrolysis at enhanced pressures (30 to 60 bars) and enhanced temperatures (100 C to 200

- C). 1984.
- [64] Tseung ACC, Jasem S. Oxygen evolution on semiconducting oxides. *Electrochim Acta* 1977;22(1):31–4.
- [65] Trasatti Sergio. Physical electrochemistry of ceramic oxides. *Electrochim Acta* 1991;36(2):225–41.
- [66] Awad MM. Two-phase flow. INTECH Open Access Publisher; 2012.
- [67] Wendt H, Plzak V. Electrocatalytic and thermal activation of anodic oxygen- and cathodic hydrogen-evolution in alkaline water electrolysis. *Electrochim Acta* 1983;28(1):27–34.
- [68] Hamdani MRNS, Singh RN, Chartier P. Co₃O₄ and Co-based spinel oxides bifunctional oxygen electrodes. *Int J Electrochem Sci* 2010;5(4):556.
- [69] Stojadinović J, Wiedenmann Daniel, Gorbar M, La Mantia F, Suarez L, Zakaznova-Herzog V, et al. Electrochemical characterization of porous diaphragms in development for gas separation. *ECS Electrochem Lett* 2012;1(4):F25–8.